J. Fluid Mech. (2022), *vol*. 949, A30, doi:10.1017/jfm.2022.762

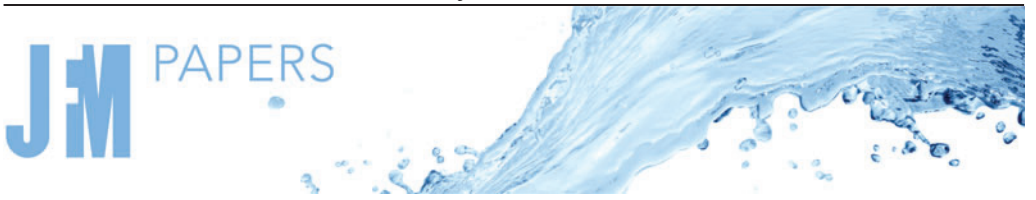

Scale-to-scale turbulence modification by small settling particles

Roumaissa Hassaini[1],† **and Filippo Coletti**[1]

[1]Department of Mechanical and Process Engineering, ETH Zurich, 8092 Zürich, Switzerland

(Received 18 May 2022; revised 18 August 2022; accepted 26 August 2022)

Despite decades of investigations, there is still no consensus on whether inertial particles augment or dampen turbulence. Here, we perform the first experimental study in which the particle concentration is varied systematically across a broad range of volume fractions Φ_v, from nominally one-way coupled to heavily two-way coupled regimes, keeping all other parameters constant. We utilize a zero-mean flow chamber where steady, homogeneous and approximately isotropic air turbulence is realized, with a Taylor-microscale Reynolds number $Re_\lambda = 150$–300. We consider spherical solid particles of two sizes, both much smaller than the Kolmogorov length, and yielding Stokes numbers $St_\eta = 0.3$ and 2.6 based on the Kolmogorov time scale. By adjusting the turbulent intensity, the settling velocity parameter is kept constant for both cases, $Sv_\eta = V_t/u_\eta \approx 3$ (where V_t is the still-air terminal velocity, and u_η is the Kolmogorov velocity scale). Unlike previous studies focused on massively inertial particles, we find that the turbulent kinetic energy increases with particle loading, being more than doubled at $\Phi_v = 5 \times 10^{-5}$. This is attributed to the energy input associated with gravitational settling: the particles release their potential energy into the fluid and increase its dissipation rate, while the time scale associated with the inter-scale energy transfer is not strongly changed. Two-point statistics indicate that the energy-containing eddies become vertically elongated in the presence of falling particles, and that the latter redistribute the energy more homogeneously across the scales compared to unladen turbulence. This is rooted in an enhanced cascade, as shown by the nonlinear inter-scale energy transfer rate.

Key words: multiphase and particle-laden flows, turbulent flows

† Email address for correspondence: rhassaini@ethz.ch

1. Introduction

Particle-turbulence interaction is a topic that has received continued attention from the scientific community for several decades (Maxey & Riley 1983; Maxey 1987; Squires & Eaton 1990, 1991; Elghobashi 1994; Crowe, Troutt & Chung 1996; Poelma & Ooms 2006; Balachandar & Eaton 2010). The coupling between continuous and dispersed phase, the number of governing parameters, and the wide range of scales, make for a formidable challenge for experimentalists and modellers alike. Driven by the practical relevance of the problem, particle-laden turbulence has attracted renewed attention in the last decade, also thanks to the tremendous progress in our ability to carry out novel measurements and simulations in previously inaccessible conditions (Monchaux, Bourgoin & Cartellier 2012; Tenneti & Subramaniam 2014; Gustavsson & Mehlig 2016; Maxey 2017; Mathai, Lohse & Sun 2020; Brandt & Coletti 2022).

One of the most elusive aspects of the problem is the back-reaction of inertial particles on the fluid, referred to as two-way coupling. Turbulence modification by particles is believed to be significant already at modest loadings, i.e. above volume fractions $\Phi_v = O(10^{-6})$ for gas–solid systems (Elghobashi 1994). However, the evidence on whether the turbulence is augmented or attenuated, and to which extent, is controversial. A dated but still utilized criterion was proposed by Gore & Crowe (1991), who compiled previous data and concluded that turbulence was augmented/attenuated by particles larger/smaller than one-tenth of the integral scale. This implies that sub-Kolmogorov particles (whose diameter d_p is smaller than the Kolmogorov scale η) will always attenuate turbulence even when it exhibits marginal scale separation, at odds with several experimental observations (e.g. Yang & Shy 2005). Some early experiments focused on wall-bounded flows, some reporting attenuation (e.g. Kulick, Fessler & Eaton 1994; Paris 2001) and others augmentation (e.g. Sato & Hishida 1996). Tanaka & Eaton (2008) compiled experimental results for turbulence modification in internal flows. They proposed a criterion based on a non-dimensional parameter combining the particle response time, density and size relative to the flow scales, as well as the flow Reynolds number, signalling the complexity of the coupling. Numerical simulations have struggled to reproduce the measurements, even when laboratory conditions were matched and the resolution was appropriate for direct numerical simulation (DNS) of the single-phase turbulence; see e.g. Vreman (2015) and Wang *et al.* (2019). This is partly attributable to the limitations of the classic point-particle method, in which particles are treated as material points applying pointwise forcing on the fluid computational grid; see Eaton (2009), Maxey (2017) and Brandt & Coletti (2022).

Studying turbulence modification in wall-bounded flows, while highly relevant to several applications, requires disentangling the simultaneous effects on the hierarchy of scales in the boundary layer (Wang & Richter 2019). Moreover, the particle–fluid slip velocity, which plays a crucial role in the momentum coupling, varies significantly with wall distance (Kiger & Pan 2002; Fong, Amili & Coletti 2019; Berk & Coletti 2020; Baker & Coletti 2021), complicating the generalization of the results. For example, Righetti & Romano (2004) found that turbulence fluctuations were enhanced in the viscous sub-layer but damped further away from the wall. Additionally, at the centre-plane of a channel flow, the turbulence is anisotropic at moderate Reynolds numbers (Andersson, Zhao & Variano 2015). Thus homogeneous isotropic turbulence may be a more suitable terrain to attack the fundamental aspects of the inter-phase coupling. This is the focus of the present investigation.

Creating homogeneous isotropic turbulence in the laboratory is notoriously challenging (Bellani & Variano 2014). The classic approach is grid-generated turbulence, which was used by Schreck & Kleis (1993), Geiss *et al.* (2004) and Poelma, Westerweel &

Ooms (2007) to investigate particle–turbulence interaction. The dispersed phase was found to induce large-scale anisotropy, with larger axial velocity fluctuations. Highly inertial particles caused mild turbulence attenuation over the entire spectrum, while particles with a Stokes number $St_\eta = \tau_p/\tau_\eta < 1$ energized the small-scale fluctuations and modulated the large-scale ones (where τ_p is the particle response time, and τ_η is the Kolmogorov time scale). The experiments of Poelma *et al.* (2007) were the first to describe clearly such 'pivoting' of the energy spectrum, which had been reported in several previous simulations (as summarized by Poelma & Ooms 2006). A similar behaviour had been observed previously in bubble-laden turbulence (Mazzitelli, Lohse & Toschi 2003*a*,*b*; Rensen, Luther & Lohse 2005).

Grid turbulence, however, presents shortcomings associated with its spatial decay, particularly the weak level of turbulent agitation; in Poelma *et al.* (2007), the Reynolds numbers based on the Taylor microscale was $Re_\lambda < 30$. Zero-mean flow turbulence chambers (usually stirred by jets) overcome this limitation and can approximate homogeneous isotropic turbulence at Reynolds numbers with substantial scale separation (Bellani & Variano 2014; Carter *et al.* 2016). They were used by Hwang & Eaton (2006*a*,*b*) and Tanaka & Eaton (2010) to show that inertial particles with $St_\eta = O(10^2)$ attenuate turbulence. On the other hand, Yang & Shy (2005) reported turbulence augmentation for $St_\eta = O(1)$. In this regime, inertial particles are known to cluster over multi-scale sets (Squires & Eaton 1991; Monchaux *et al.* 2012; Gustavsson & Mehlig 2016; Baker *et al.* 2017), which may affect the two-way coupling. A zero-mean flow turbulence chamber was also used by Bellani *et al.* (2012) to investigate large, nearly neutrally buoyant particles. They observed moderate turbulence attenuation and pivoting of the energy spectrum. Those experimental findings were enabled by advances in particle image velocimetry (PIV) and particle tracking velocimetry (PTV), in particular their simultaneous application to capture the fluid flow and particle motion, respectively (Kiger & Pan 2000; Khalitov & Longmire 2002; Poelma, Westerweel & Ooms 2006).

Under the action of gravity, particles of different sizes and densities will fall at different speeds. This has far-reaching consequences for the fluid dynamics, as soon as the still-fluid terminal velocity $V_t = \tau_p g$ is comparable to some velocity scale of the turbulence (i.e. when the settling velocity parameter $Sv_\eta = V_t/u_\eta$ is not vanishingly small, where u_η is the Kolmogorov velocity scale); see Good *et al.* (2014) and Petersen, Baker & Coletti (2019). Particle inertia (i.e. the finite response time to fluid fluctuations, quantified by St_η) and gravity (i.e. the drift through the flow with crossing of fluid trajectories, quantified by Sv_η) are known to have competing effects on dispersion (Wang & Stock 1993; Berk & Coletti 2021); but the way their balance affects the turbulence is poorly understood. In a unique microgravity experiment, Hwang & Eaton (2006*b*) found that turbulence attenuation was stronger than in terrestrial gravity, pointing to the role of the particle potential energy in the fluid energy balance (Hwang & Eaton 2006*a*).

Compared to the few experimental works, many more numerical studies have considered DNS of homogeneous isotropic turbulence two-way coupled with inertial particles (Squires & Eaton 1990; Elghobashi & Truesdell 1993; Boivin, Simonin & Squires 1998; Sundaram & Collins 1999; Ferrante & Elghobashi 2003; Frankel *et al.* 2016; Saito, Watanabe & Gotoh 2019; among others), often reporting the pivoting effect mentioned above. The cross-over scale at which fluid energy was enhanced/damped by the particles often appeared to depend on St_η, and so did the answer to the augmentation/attenuation question Poelma & Ooms (2006). Still, several authors indicated multiple reasons why these results should be interpreted with caution. First, in many cases, steady-state turbulence was forced. Lucci, Ferrante & Elghobashi (2010) argued that this is not

a correct approach to study two-way coupling, independently on the type of forcing: spectral-space forcing at low wavenumbers causes wide amplitude oscillations of the turbulent kinetic energy, which cannot be distinguished from the particle back-reaction, while physical-space forcing continually modifies the spectrum to maintain a constant turbulent kinetic energy, opposing the pivoting action of the particles. Simulations of decaying turbulence are free from this problem, but suffer limitations similar to grid turbulence experiments, and can be compared only qualitatively against steady-state measurements. Second, the common point-particle forcing on the fluid computational grid presents well-known technical challenges (Eaton 2009; Brandt & Coletti 2022). Recent efforts to address the issue show promising results (Capecelatro & Desjardins 2013; Subramaniam *et al.* 2014; Gualtieri *et al.* 2015; Horwitz & Mani 2016, 2018; Ireland & Desjardins 2017; Balachandar, Liu & Lakhote 2019), but one-to-one comparisons with experiments are lacking. Third, most of those studies neglected the effect of gravity. The few DNS studies considering settling particles have reported contrasting outcomes. For the same range of parameters (density ratios of $O(10^3)$) and volume fractions of $O(10^{-5})$, Bosse, Kleiser & Meiburg (2006) found the turbulent kinetic energy to be attenuated; Frankel *et al.* (2016) and Rosa, Pozorski & Wang (2020) found that it was augmented; and Monchaux & Dejoan (2017) found that it was almost unaffected.

Arguably, particle-resolved simulations (Tenneti & Subramaniam 2014) are needed to fully capture the particle-turbulence interaction. Driven by progress in numerical strategies and ever-increasing computational power, applications of this approach flourished in recent years and have allowed new insight in the inter-phase dynamics at the particle scale (e.g. Burton & Eaton 2005; Lucci *et al.* 2010; Naso & Prosperetti 2010; Cisse, Homann & Bec 2013; Uhlmann & Doychev 2014; Fornari, Picano & Brandt 2016; Schneiders, Meinke & Schröder 2017; Wang, Abbas & Climent 2017; Mehrabadi *et al.* 2018). The level of detail gained by such computations can hardly be achieved by experiments, especially because the simultaneous measurements of particle and fluid motion in three dimensions is generally beyond reach (Guala *et al.* (2008) and Ni *et al.* (2015) being notable exceptions). Still, the range of accessible parameters for fully resolved simulations has been relatively narrow, with particles typically much larger than the Kolmogorov scales, and/or immersed in weak/decaying turbulence.

Considering the above, while the progress in the last decade is undeniable, the conclusion of the review by Balachandar & Eaton (2010) remains topical: the 'mechanisms of turbulence modulation and their parametric dependence are poorly understood and are wide open for fundamental investigation'. In a previous review, Poelma & Ooms (2006) recognized the multiplicity of important factors and called for systematic experimental studies in which one parameter at a time is varied; but no such effort has been carried out yet. We recently presented extensive measurements of particle–turbulence interaction in a homogeneous turbulence chamber, spanning a wide range of St_η, Sv_η, Re_λ and Φ_v (Petersen *et al.* 2019; Berk & Coletti 2021). Due to the interdependence of the parameters and the focus on the dispersed phase, the turbulence modification was barely addressed.

Here, we present novel measurements in the same laboratory facility, where we systematically increase the loading of heavy sub-Kolmogorov particles, keeping the other input parameters (forcing of the turbulence and particles' properties) constant. We repeat that for two values of St_η, smaller and larger than unity, keeping the same settling velocity parameter Sv_η. We leverage multi-scale, time-resolved imaging of both phases by PIV/PTV to simultaneously resolve all relevant scales of motion, and establish how the increasingly concentrated particles transform the fluid turbulence in which they settle. We report several novel findings. First, in the present range of physical parameters, the

turbulent kinetic energy is increased substantially by the presence of falling particles, roughly in proportion to the energy input rate associated with their potential energy being released into the flow. Moreover, the energy-containing eddies become elongated in the direction of gravity, although the horizontal velocity fluctuations are more strongly excited than the vertical ones. Finally, the pivoting of the energy spectrum is due to the particles inducing an enhancement of the turbulence cascade. The paper is organized as follows. Section 2 describes the experimental methodology and qualifies the flow conditions. Section 3 presents the results, detailing how the turbulence is impacted at the different scales. Section 4 summarizes the findings and draws conclusions.

2. Methods

2.1. *Experimental apparatus and parameters*

The turbulence chamber was introduced in Carter *et al.* (2016) and qualified further in Carter & Coletti (2017, 2018). Here, we only summarize the main features. It consists of a $5\,\mathrm{m}^3$ enclosure where two facing walls accommodate jet arrays activated in randomized sequence, following the original concept of Variano and co-workers (Variano, Bodenschatz & Cowen 2004; Variano & Cowen 2008; Bellani & Variano 2014). While several other random-jet-array facilities have since been build (Mydlarski 2017), the present chamber is the only one using air as working fluid and was specifically designed to study the interaction of inertial particles with homogeneous turbulence. It is especially suitable for this goal because in the central portion of the chamber: (i) the mean flow is much smaller than the root-mean-square (r.m.s.) velocity fluctuations; (ii) the turbulence is statistically homogeneous over a region much larger than the energetic scales; (iii) the spatial gradients of the mean velocity are negligible; and (iv) the attainable Reynolds numbers are sufficient to reach power-law (Kolmogorov 1941) scaling of the velocity structure functions. The intensity and isotropy of the turbulence can be adjusted by varying the average jet firing time and the distance between the jet arrays, and by adding grids in front of the jets (Carter *et al.* 2016).

Petersen *et al.* (2019) and Berk & Coletti (2021) used this facility to investigate clustering and settling of inertial particles, and we adopt a similar set-up. The inertial particles (size-selected spherical glass micro-beads of density $\rho_p = 2500\,\mathrm{kg\,m^{-3}}$) are dropped through a 3 m vertical chute and enter the chamber through a 152 mm circular opening in the ceiling. With respect to those previous studies, we release the particles with an hourglass system instead of a screw-feeder, ensuring continuous feeding and precise control of the mass flow rate. Therefore, we are able to adjust and systematically vary the mass loading. Visual inspection and PIV/PTV imaging confirm that the air turbulence spreads the falling particles over a large fraction of the chamber volume, with no significant variation of spatial concentration over the homogeneous turbulence region or in the field of view (FOV) of the imaging (Petersen *et al.* 2019). The mean vertical velocity of the air remains much smaller ($\lessapprox 10\,\%$) than its r.m.s. fluctuations for all considered particle volume fractions.

We consider two combinations of particle and turbulence properties (in single-phase realization), summarized in table 1. In both cases, the particles have sub-Kolmogorov size and lie in the $St_\eta = O(1)$ range for which clustering is expected. The response time τ_p is calculated with the Schiller–Naumann correction (Clift, Grace & Weber 2005). The Reynolds number based on the still-air terminal velocity $Re_{p,t} = d_p V_t/\nu$ (where ν is the air kinematic viscosity) is smaller than unity, thus negligible particle wakes are expected.

The ratio u_1'/u_3' indicates approximate large-scale isotropy. The integral scale and the turbulence dissipation are obtained from two-point velocity correlations and second-order velocity structure functions, as discussed in § 3. To isolate the effect of particle inertia and gravity, the settings are chosen to yield two different St_η and similar Sv_η. Under fixed gravity, this necessarily requires varying Re_λ between the cases. While we expect the results to be more sensitive to St_η than Re_λ over the considered range, we will refrain from inferring quantitative Stokes number trends from our data. In fact, the numerical simulations by Tom & Bragg (2019) indicate that for the present range of St_η, the settling dynamics can be very sensitive to Re_λ. Overall, both cases show similar behaviours, and comparisons will rather serve as an indication that the conclusions hold over the present range of parameters. For simplicity, throughout the paper we will refer to both configurations as the $St_\eta = 0.3$ case and $St_\eta = 2.6$ case, respectively. The volume fraction Φ_v and mass fraction $\Phi_m = \Phi_v \rho_p/\rho_f$ (where ρ_f is the air density) span ranges in which the back-reaction on the turbulence is expected to vary from marginal to substantial (Elghobashi 1994; Balachandar & Eaton 2010). As the particles alter the flow, several observables will change, including the fluid velocity fluctuations and the fall speed of the particles themselves. In order to characterize the system, the parameters reported in table 1 are defined for the baseline configuration unaffected by two-way coupling.

2.2. *Measurement techniques*

In the following, x_1 indicates the horizontal direction parallel to the jet axes, x_2 is horizontal and perpendicular to x_1, and x_3 is vertical; the respective fluid velocity components are U_1, U_2 and U_3. Fluctuating fluid velocities are denoted by $u_i = U_i - \overline{U_i}$, where the subscript i indicates the ith component, and the overbar indicates temporal averaging. Angle brackets indicate space–time averaging, and a prime indicates r.m.s fluctuations. The subscript p denotes quantities related to the particles.

We perform simultaneous PIV on the fluid phase and PTV on the particle phase. The method is similar to that described in Petersen *et al.* (2019) and Berk & Coletti (2021); only salient differences are addressed here. Time-resolved imaging is carried out using an Nd:YLF single-pulse laser (Photonics, 30 mJ pulse^{-1}) operated at 4 kHz to illuminate a vertical (x_1, x_3)-plane at the centre of the chamber. Two synchronized CMOS cameras (Phantom VEO, active sensor of 1280 by 1280 pixels) image the in-plane air motion through DEHS tracers seeding the chamber, and track the inertial particles about 90 cm below the ceiling opening. The images are separated into 'tracers only' and 'particles only', with a routine that we described in detail in Petersen *et al.* (2019) and applied recently to various particle-laden turbulent flows (Fong *et al.* 2019; Berk & Coletti 2020; Baker & Coletti 2021).

Figure 1 illustrates a sample instantaneous realization of the two-phase flow. The fluid velocity is measured by PIV via iterative cross-correlation of successive image pairs, with a final interrogation window size of 24 × 24 pixels and 50 % overlap. The imaging and PIV specifications are reported in table 2. To qualify the spatio-temporal scales resolved by the measurements, we refer to the single-phase flow properties in table 1. Both cameras are operated simultaneously and capture two nested fields of view, enhancing the dynamic range of the measurements. One camera mounts a 105 mm Nikon lens (f# 5.6), yielding a FOV large enough to capture the integral length scales. The other mounts a 200 mm Nikon lens (ff# 4) and approximately resolves the Kolmogorov length scales: the vector spacing is about η and 4η at the lower and higher Re_λ, respectively. The acquisition frequency resolves 19 to 96 times the Kolmogorov time scales, again depending on Re_λ.

https://doi.org/10.1017/jfm.2022.762 Published online by Cambridge University Press

d_p (μm)	τ_p (ms)	$Re_{p,t}$	St_η	Sv_η	u_1' (m s^{-1})	u_1'/u_3'	$L_{1,1}$ (mm)	ϵ (m^2 s^{-3})	η (mm)	τ_η (ms)	Re_λ	Φ_v	Φ_m
32	7.4	0.15	0.3	2.8	0.15	1.16	79	0.03	0.58	22	152	10^{-6}–4×10^{-5}	2×10^{-3}–8.4×10^{-2}
52	17	0.56	2.6	3.5	0.39	1.21	120	0.35	0.31	7	289	10^{-6}–5×10^{-5}	2×10^{-3}–1.5×10^{-1}

Table 1. Properties of the particles and the turbulence (for the unladen flow case) for both investigated configurations. Here, d_p and τ_p are the particle diameter and response time; $Re_{p,t}$ is the particle Reynolds number based on the terminal velocity; St_η and Sv_η are the Stokes number and settling velocity parameter based on Kolmogorov scales; u_1' and u_3' are the r.m.s. fluid velocity fluctuations in the horizontal and vertical directions, respectively; $L_{1,1}$ is the integral scale of the turbulence in the horizontal direction; ϵ is the turbulent dissipation calculated from the second-order velocity structure function; η and τ_η are the Kolmogorov length and time scales; Re_λ is the Taylor-microscale Reynolds number of the turbulence; and Φ_v and Φ_m are the volume and mass fraction of the particles, respectively.

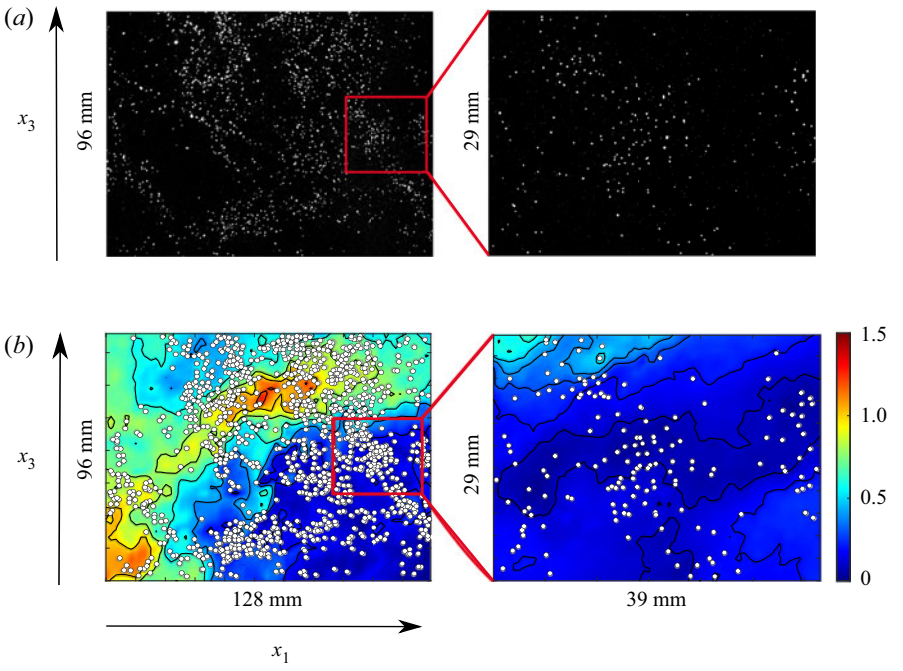

Figure 1. (*a*) Example of nested raw images of the particle-laden flow, captured in the large (left) and small (right) field of view (FOV) for $St_\eta = 2.6$. (*b*) The corresponding in-plane fluid velocity in $\mathrm{m\,s^{-1}}$ (colour contours) and particle positions (white dots, not in scale size).

	Lens focal length (mm)	Field of view (mm × mm)	Resolution (pixel mm^{-1})	PIV vector spacing (mm)
Small FOV	200	39 × 29	33	0.36
Large FOV	105	128 × 96	10	1.2

Table 2. Imaging parameters for the small and large field of view (FOV).

Besides considerations about the scales of the flow, the camera resolutions and inter-frame separations are optimized so that the tracer displacements are suitable for velocimetry in both cameras: these are approximately 4 and 9 pixels for the large and small FOV, respectively. For each volume fraction, 10 runs of 43 000 successive images are obtained, for a total measurement time of 100 s or approximately 500 integral time scales (defined below).

The detected particle count in the illuminated volume is used to calculate the volume fraction Φ_v; see Petersen *et al.* (2019) and Fong *et al.* (2019), where the approach could be validated in a vertical channel flow with known particle mass loading. Over the present range of Φ_v, the fluid turbulence can be characterized with sufficient image quality for successful processing. This is based on the extensive analysis of the phase separation by Petersen *et al.* (2019), where similar regimes and volume fractions were reached. In particular, the systematic variation of Φ_v in the present study allows us to verify that the occurrence of non-valid PIV vectors is not correlated with the presence of inertial particles in a given interrogation window. The PIV random error in the small FOV (where

the spatial resolution is sufficient to capture the Kolmogorov scales of the single-phase turbulence) is estimated by extrapolating the two-point correlation to vanishing separation (Adrian & Westerweel 2011) and is found to be less than 1 % of the velocity variance. The dominant source of uncertainty on the flow statistics is thus the finite sample size. Convergence tests show that each run is well converged for all considered observables, while run-to-run variation is larger. In the following, where appropriate, the standard deviation of the various runs will be used to indicate error bars.

A specific feature of the present zero-mean flow facility is the spatial homogeneity over scales much larger than the integral scale, for both fluid and particle statistics (Carter *et al.* 2016; Carter & Coletti 2017, 2018; Petersen *et al.* 2019). This allows drawing more general conclusions compared to systems in which wall proximity and spatial gradients cause dependence on the boundary conditions. Moreover, the considered particles have reached terminal velocity well before entering the region of interest, as indicated by their negligible mean vertical acceleration (see Berk & Coletti 2021). Finally, the lack of significant mean flow (especially small in the vertical direction) further limits the possible influence from portions of the volume outside the region of interest. In other words, in the considered central region of the chamber, the integral scale of the turbulence sets the scale over which spatial gradients of the flow properties have an influence. Therefore, the flow condition outside the FOV are not expected to alter the statistics measured in the imaging window, which is of the order of the integral scale and about one metre removed from the chamber walls.

Figure 2 displays the time record of instantaneous Φ_v, u_1' and $u_{1,p}'$ during a sample run for the case $St_\eta = 2.6$ at volume fraction 4×10^{-5}. Beyond the large-scale excursions, the plots confirm the steady-state behaviour of both phases. We will use the local particle concentration, velocity and fluid velocity at the particle location (interpolated as in Petersen *et al.* 2019; Berk & Coletti 2021), extracted from the small-FOV measurements, to estimate the extra dissipation caused by the particles; see § 3.2. The local concentration is obtained by Voronoi tessellation of the particle field (Monchaux, Bourgoin & Cartellier 2010).

3. Results

3.1. *Large-scale turbulence properties*

The results in this section are obtained from the large-FOV measurements. We begin by considering the effect of the particles on the r.m.s. velocity fluctuations of the turbulence. Figure 3(*a*) shows the laden-to-unladen ratio for the horizontal component, $u_1'/u_{1,\Phi=0}'$, for the different volume fractions. A monotonically increasing trend is apparent for both Stokes numbers, with the larger St_η case displaying a stronger increase. The vertical component also increases with volume fraction, but less than the horizontal one. Indeed, the anisotropy ratio u_1'/u_3' grows significantly over the considered range of volume fractions (figure 3*b*), the growth being again stronger for $St_\eta = 2.6$ than for $St_\eta = 0.3$.

The enhancement of the r.m.s. fluid velocity fluctuations in both directions indicates that the turbulent kinetic energy (TKE) is augmented significantly by the presence of the particles, as we will discuss later. Moreover, the fact that the particle-laden turbulence fluctuations are more intense in the horizontal than in the vertical direction is at odds with previous numerical studies: simulations of decaying (Ferrante & Elghobashi 2003) and forced (Bosse *et al.* 2006) homogeneous turbulence found that the addition of settling particles resulted in anisotropy ratios $u_1'/u_3' < 1$. Also, the grid turbulence measurements of Geiss *et al.* (2004) and Poelma *et al.* (2007) showed stronger fluid fluctuations in the

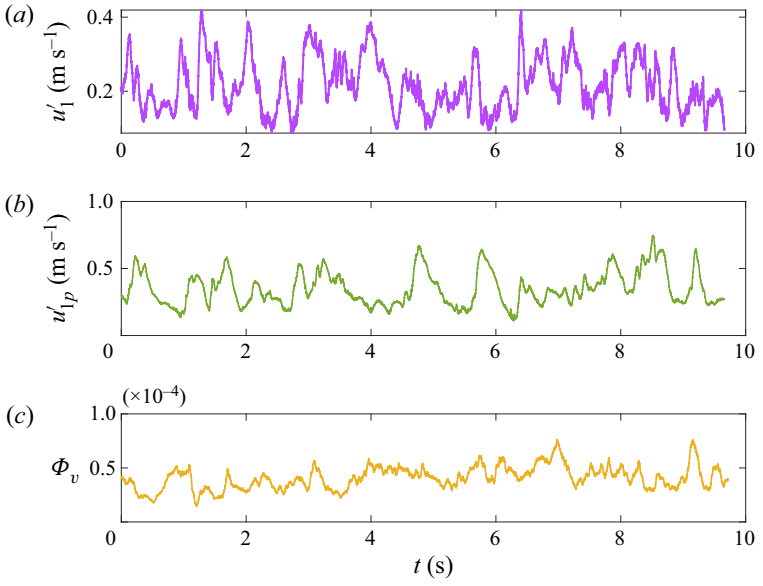

Figure 2. Temporal evolution of spatially averaged quantities during one experimental run for the case $St_\eta = 2.6$ with mean volume fraction 4×10^{-5}. The instantaneous volume fraction Φ_v, the r.m.s. of the horizontal flow velocity fluctuations, u_1', and the r.m.s. of the horizontal particle velocity fluctuations, u_{1p}', are displayed. The data are from the large FOV.

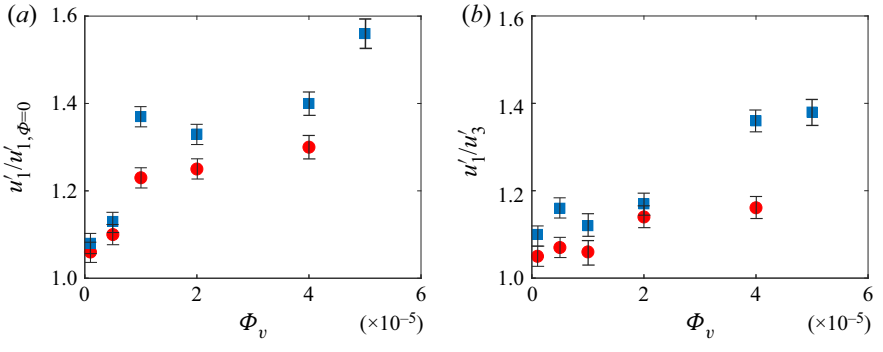

Figure 3. (*a*) The r.m.s. of the horizontal velocity fluctuation as a function of the particle volume fraction, normalized by the one measured in the unladen flow. (*b*) Ratio between the horizontal and the vertical r.m.s. fluctuations, as a function of the particle volume fraction. Squares indicate the $St_\eta = 2.6$ case, and circles indicate the $St_\eta = 0.3$ case. The data are from the large FOV.

direction of gravity than in the transverse direction. However, direct comparison with these experiments is hampered by the differences in parameters compared to the present case: the particles in Geiss *et al.* (2004) were quasi-ballistic, while those in Poelma *et al.* (2007) were not small compared to the Kolmogorov scales, and produced wakes with large momentum deficit, which heavily impacted their weak decaying turbulence.

The influence of the settling particles on the large-scale turbulence properties is further illustrated by the integral scales, obtained from the spatial autocorrelation of the velocity

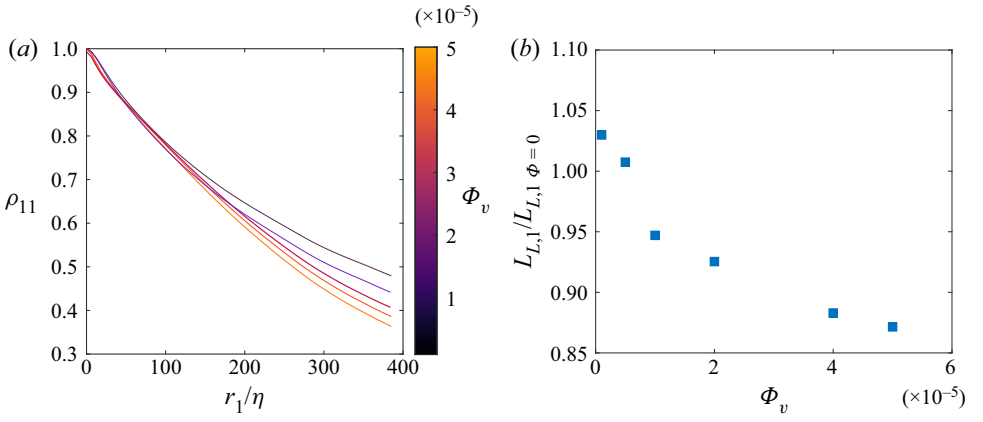

Figure 4. (*a*) Autocorrelation coefficient of the horizontal velocity fluctuations at the different volume fractions for $St_\eta = 2.6$. (*b*) Corresponding longitudinal integral scale, normalized by the unladen case, as a function of the particle volume fraction. The data are from the large FOV.

fluctuations:

$$\rho_{ii}(\boldsymbol{r}) = \frac{\langle u_i(\boldsymbol{r})\, u_i(\boldsymbol{x}+\boldsymbol{r})\rangle}{\langle u_i(\boldsymbol{x})^2\rangle}, \tag{3.1}$$

where x and r are the position and separation vectors, respectively, and no index summation is implied. In general, the integral length scales associated with fluctuations u_i over separations r_j are defined as

$$L_{i,j} = \int_0^{r_0} \rho_{ii}(r_j)\,\mathrm{d}r, \tag{3.2}$$

where r_0 is the first zero crossing of ρ_{ii}. In practice, the extent of the integration is limited by the size of the imaging window, and therefore we take as conventional estimate the separation at which the correlation function drops below 0.5. Other common methods such as extrapolating an exponential fit yield similar results. As in Carter & Coletti (2017), we define the integral and transverse scales as $L_{L,1} = L_{1,1}$ and $L_{T,1} = L_{1,2}$, respectively. The subscript 1 indicates that we use the horizontal component of the velocity, the vertical one returning similar trends.

In figure 4(*a*), we show the autocorrelation of the horizontal velocity fluctuations along the horizontal separation, ρ_{11}, for the $St_\eta = 2.6$ case. The correlation decays faster with increasing volume fraction, which results in a drop of the longitudinal integral scale $L_{L,1}$ as shown in figure 4(*b*). As we already remarked, u_1' increases with volume fraction, so the shrinking of the integral scale suggests that the falling particles subtract energy from the large scales and inject it at the small scales, with a positive global balance (i.e. a net increase of TKE). This view will be confirmed in the following sections.

To better appreciate the particle influence on the large-scale spatial structure of the turbulence, we plot in figure 5(*a*) the 0.5 contours of ρ_{11} in the (r_1, r_2)-plane. With increasing volume fraction, the horizontal extent of the correlation area shrinks, decreasing $L_{L,1}$ as mentioned; instead, its vertical extent grows, increasing the transverse length scale $L_{T,1}$. This is quantified in figure 5(*b*), showing the $L_{L,1}/L_{T,1}$ ratio as a function of volume fraction. For the single-phase case, the ratio departs from the canonical value 2 due to incomplete homogeneity and isotropy across the FOV. The ratio shows a clear decreasing trend with increasing particle loading. The 0.5 contours of the

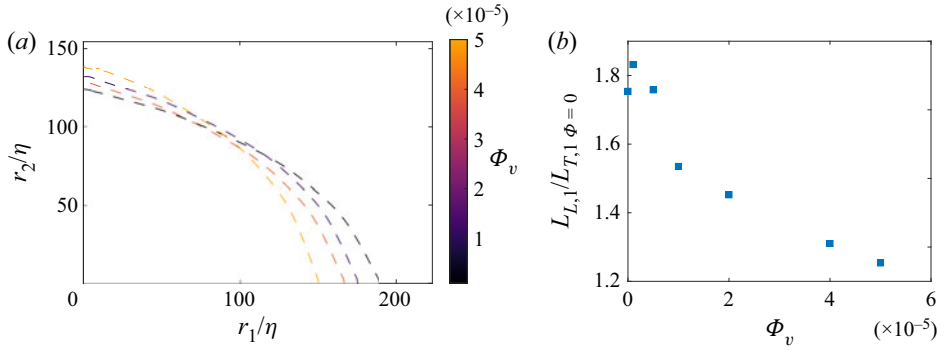

Figure 5. (*a*) Contours of the autocorrelation coefficient ρ_{11} in the two-dimensional scale space (r_1, r_2) for the case $St_\eta = 2.6$ at different volume fractions. (*b*) Corresponding ratio between the longitudinal and transverse integral scales, as a function of the particle volume fraction. The data are from the large FOV.

vertical velocity autocorrelation ρ_{22} (not shown for brevity) display a similar vertical stretch, with an increase of the longitudinal length scale ($L_{L,2} = L_{2,2}$) and decrease of the transverse length scale ($L_{T,2} = L_{2,1}$). Taken together, these results indicate that the energy-containing eddies become elongated vertically in the presence of falling particles at increasing concentrations. This contrasts with the above observation that the horizontal fluid fluctuations are excited more than the vertical ones: in single-phase turbulence, the integral scales are stretched in the direction along which fluctuations are more intense (Carter & Coletti 2017). The presence of the particles clearly alters the way energy is redistributed between different directions and across scales.

3.2. *Turbulent kinetic energy and dissipation rate*

As anticipated in the previous subsection, the presence of particles in the present regime augments the turbulent kinetic energy of the carrier fluid. This is evident in figure 6, where we plot TKE calculated as

$$\mathrm{TKE} = \tfrac{1}{2}(2u_1'^2 + u_3'^2) \tag{3.3}$$

from the large- and small-FOV data at different volume fractions. In (3.1), we assume that the out-of-plane velocity variance is equal to the measured horizontal component. This is expected when the baseline single-phase turbulence is approximately isotropic, which is justified by the value of u_1'/u_3' in absence of particles (table 1). The change in TKE compared to the single-phase flow is marginal for $\Phi_v \approx 10^{-6}$, in agreement with the order-of-magnitude estimate of Elghobashi (1994). The turbulence is augmented monotonically with increasing volume faction, leading to TKE increases of 70 % at $\Phi_v = 4 \times 10^{-5}$ for $St_\eta = 0.3$, and more than 150 % at $\Phi_v = 5 \times 10^{-5}$ for $St_\eta = 2.6$. Such a dramatic augmentation of turbulence is in stark contrast with the criterion of Gore & Crowe (1991) and with several previous experimental studies: Paris (2001), Hwang & Eaton (2006*a*,*b*) and Tanaka & Eaton (2008) found that solid particles attenuated air turbulence. Those authors, however, considered significantly more inertial particles ($St_\eta \approx 50$–100), and in the following we reason that this is the likely cause of the different behaviour.

The increase in TKE is related to the energy balance in the particle-laden turbulence, where gravitational settling plays a major role: as the particles fall, they transfer potential

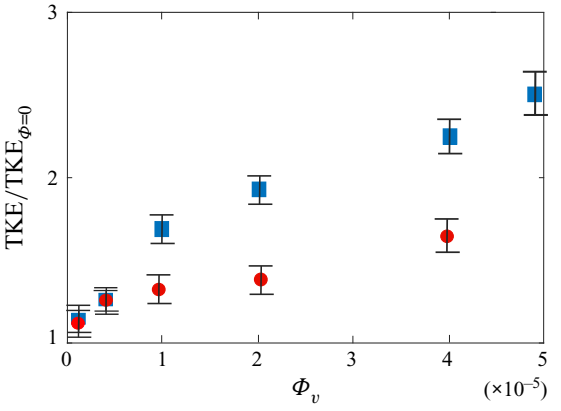

Figure 6. Turbulent kinetic energy normalized by the unladen case, as a function of the particle volume fraction. Squares indicate the $St_\eta = 2.6$ case, and circles indicate the $St_\eta = 0.3$ case. The data are from the small FOV.

energy into the flow. Following Hwang & Eaton (2006*a*), we consider the steady-state energy budget

$$E_j + E_g = \epsilon + \epsilon_p, \tag{3.4}$$

where the left-hand and right-hand sides represent the energy per unit time, and mass injected and dissipated in the fluid control volume, respectively. Here, E_j is the forcing from the jets, which is independent of the mass loading and equals the energy dissipation rate in the single-phase cases. The energy per unit time released by the falling particles is $E_g = \Phi_m \langle U_{3,p} \rangle g$, analogous to estimates for rising bubbles (Riboux, Risso & Legendre 2010; Risso 2018). The viscous dissipation of turbulence energy due to the cascade from larger to smaller eddies, ϵ, is estimated by evaluating directly the in-plane velocity gradients resolved by PIV from the small FOV (see De Jong *et al.* 2009; Carter *et al.* 2016). For single-phase turbulence in this facility imaged with similar parameters, such a direct estimate was shown to agree closely with the one based on velocity structure functions (Carter *et al.* 2016; Carter & Coletti 2017, 2018). The presence of the particles leads to an extra dissipation ϵ_p associated with their interaction with the fluid, in particular the boundary layer around the particles, which is far below the PIV resolution limits. This can be estimated with the classic expression proposed by Elghobashi & Abou-Arab (1983) and used in several later studies (Rogers & Eaton 1991; Kulick *et al.* 1994; Hwang & Eaton 2006*a*; Sahu, Hardalupas & Taylor 2016; among others):

$$\begin{aligned}\epsilon_p = {} & \frac{\langle C \rangle}{\rho_f \tau_p} \left(\langle u_{i,fp} u_{i,fp} \rangle - \langle u_{i,fp} u_{i,p} \rangle \right) + \frac{1}{\rho_f \tau_p} \left(\langle c u_{i,fp} u_{i,fp} \rangle - \langle c u_{i,fp} u_{i,p} \rangle \right) \\ & + \frac{1}{\rho_f \tau_p} \left(\langle U_{i,fp} \rangle - \langle U_{i,p} \rangle \right) \langle c u_{i,fp} \rangle. \end{aligned} \tag{3.5}$$

Here, C and c correspond to the local particle concentration and the local particle concentration fluctuation, and u_{fp} is the fluid velocity fluctuation at the particle location.

Figure 7(*a*) shows ϵ_p as a function of volume fraction (normalized by the unladen turbulence dissipation, $\epsilon_{\Phi=0}$) evaluated in two ways: indirectly from (3.4) as $E_j + E_g - \epsilon$, and directly from (3.5). The results are displayed for $St_\eta = 2.6$, the outcome for $St_\eta = 0.3$ being analogous. Both methods show a similar trend, although with discrepancies at

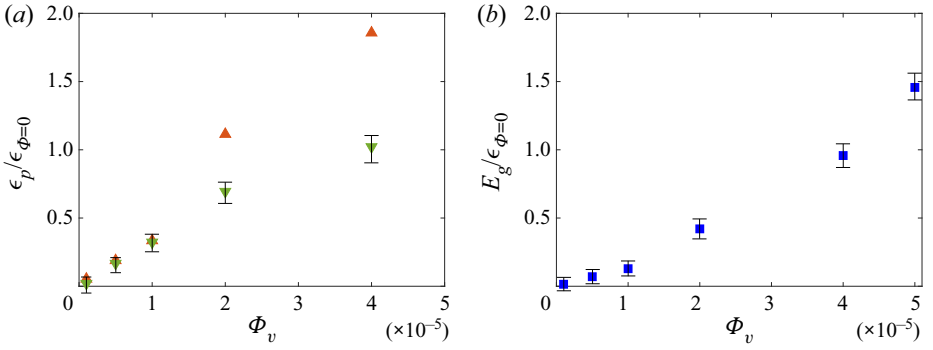

Figure 7. (*a*) Particle-induced dissipation $\epsilon_p(a)$, and (*b*) gravitational energy input rate $E_g(b)$, both normalized by the turbulent dissipation of the unladen flow, for $St_\eta = 2.6$. In (*a*), upward-pointing triangles and downward-pointing triangles represent estimates of ϵ_p from (3.5) and (3.4), respectively. The data point from (3.5) at the highest concentration was discarded, due to the uncertainty in estimating the high-order terms. The data are from the small FOV.

higher loadings. We remark that an accurate evaluation of ϵ_p, following either method, is highly challenging for several reasons. First, the evaluation of ϵ in presence of suspended particles is even more difficult than in unladen turbulence (where it is already notoriously difficult). Second, (3.4) is based on the assumption that the forcing from the jets is independent of the presence of the particles, while the latter could indirectly influence the amount of kinetic energy injected at large scales in the investigated region. Third, and perhaps most important, (3.5) is based on the same assumptions as two-way-coupled point-particle models (Hwang & Eaton 2006*a*), which have well-known shortcomings resulting in epistemic uncertainties that are hard to quantify. Indeed, the error bars representing statistical variability are not displayed for ϵ_p based on (3.5), as this is not the main source of error. Despite those limitations, both estimates of ϵ_p in figure 7(*a*) lead to a clear observation: at the larger considered volume fractions, the extra dissipation due to the particles becomes of the order of the baseline dissipation. Likewise, the energy input E_g associated with gravitational settling, shown in figure 7(*b*) for the same case, also increases with Φ_v and becomes comparable to $\epsilon_{\Phi=0}$. The increase is due not only to the mass loading itself, but also to the mean settling velocity, which grows by 110 % over the considered range of volume fractions. This may be due to collective drag effects (as indicated by Bosse *et al.* 2006) or preferential sweeping (which was shown to remain important in recent two-way-coupled simulations by Tom, Carbone & Bragg 2022). The analysis of the settling enhancement is beyond the scope of the present work and will be addressed in detail in a separate study. The important observation is that gravitational settling contributes majorly to the amount of energy injected and dissipated in the fluid per unit time. Whether TKE also increases is related to the time scale over which the dissipation is expressed. Tanaka & Eaton (2010) pointed out how both the turbulence integral time scale and the particle response time may be appropriate candidates. The latter does not vary with the particle loading, while the former (taken as L_L/u', averaging between horizontal and vertical components) increases by at most ≈30 % for the higher Φ_v. Thus, as the time scale is not drastically changed by the presence of the particles, at steady state we can expect the turbulent kinetic energy of the system to rise with particle loading, as observed.

This type of reasoning was used by Hwang & Eaton (2006*a*) to argue that settling contributed to augmenting turbulence also in their system; but that was not sufficient to

offset the ability of their quasi-ballistic particles to act as sinks of fluid momentum. Their microgravity experiments (Hwang & Eaton 2006*b*) confirmed such an argument, showing larger turbulence attenuation compared to an equivalent particle-laden turbulence regime under terrestrial gravity. Recently, Saito *et al.* (2019) used two-way coupled simulations to show that massively inertial point-particles (akin to fixed obstacles in the flow) severely attenuated turbulence, while the effect was much weaker for less inertial particles that more closely follow the flow. According to such a view, the difference between the present observations and those from Eaton and co-workers (Paris 2001; Hwang & Eaton 2006*a*,*b*; where $St_\eta \approx 50$–100) can be attributed to the smaller Stokes number in our system. Indeed, the one previous experimental study with solid particles in air at $St_\eta = O(1)$ also found turbulence augmentation (Yang & Shy 2005).

The natural question is why the settling of $St_\eta = O(1)$ particles excites turbulence more than the settling of quasi-ballistic ones. A possible explanation is suggested by a comparison with bubble-laden turbulence. Mazzitelli *et al.* (2003*a*,*b*) found numerically that small rising bubbles accumulate in the downward side of turbulent eddies due to the lift force (as recently confirmed experimentally by Salibindla *et al.* 2020), transferring momentum upwards, which enhances their ability to modify the turbulence. Likewise, small heavy particles with $St_\eta = O(1)$ form clusters that oversample downward regions of the flow (Wang & Stock 1993; Baker *et al.* 2017; Petersen *et al.* 2019), and therefore they may locally enhance turbulent fluctuations more effectively than ballistic particle that do not cluster. This interpretation is consistent with the larger TKE increase for particles with $St_\eta > 1$, which experience stronger clustering than those with $St_\eta < 1$ under the action of gravity (Matsuda, Onishi & Takahashi 2017; Petersen *et al.* 2019).

As mentioned in the Introduction, although numerous authors investigated two-way coupling of point-particles, only a few of them included gravity in forced homogeneous turbulence. Bosse *et al.* (2006) found turbulence attenuation by particles with $St_\eta \approx Sv_\eta \approx 1$, while Frankel *et al.* (2016) considered faster falling particles ($St_\eta = 1.6$ and $Sv_\eta = 6.8$) and reported an increase of TKE consistent with our observations. Besides the limitations of the point-particle approach, these comparisons with simulations also support the view that gravitational settling enhances the turbulence activity in the carrier flow.

3.3. *Turbulence modification across scales*

The change in TKE is the result of turbulence modification over the entire spectrum. Figure 8 shows the longitudinal second-order velocity structure function, which, compared to the Fourier spectrum, is less sensitive to finite-sample biases (Rensen *et al.* 2005; De Jong *et al.* 2009) and to missing data that may result from the presence of particles (Poelma & Ooms 2006). We consider the second-order structure function

$$D_{ii}(\boldsymbol{r}) = \langle [u_i(\boldsymbol{x}+\boldsymbol{r}) - u_i(\boldsymbol{x})]^2 \rangle, \tag{3.6}$$

where $\boldsymbol{x}$ is the position vector, and $\boldsymbol{r}$ is the separation vector. We focus on the longitudinal structure functions, where the velocity component is parallel to the separation vector, particularly on $D_{11}(r_1)$, $D_{22}(r_2)$ and the transverse structure functions showing the same behaviour. According to Kolmogorov theory (Kolmogorov 1941), (3.6) scales as $(\epsilon r)^{2/3}$ for separations in the inertial range. Although the considered range of Re_λ possesses limited scale separation, Carter *et al.* (2016) and Carter & Coletti (2017) showed, and the present data confirm, that the single-phase turbulence in this facility approximately follows Kolmogorov scaling in the range $r \approx 20\eta$–50η. The addition of particles alters

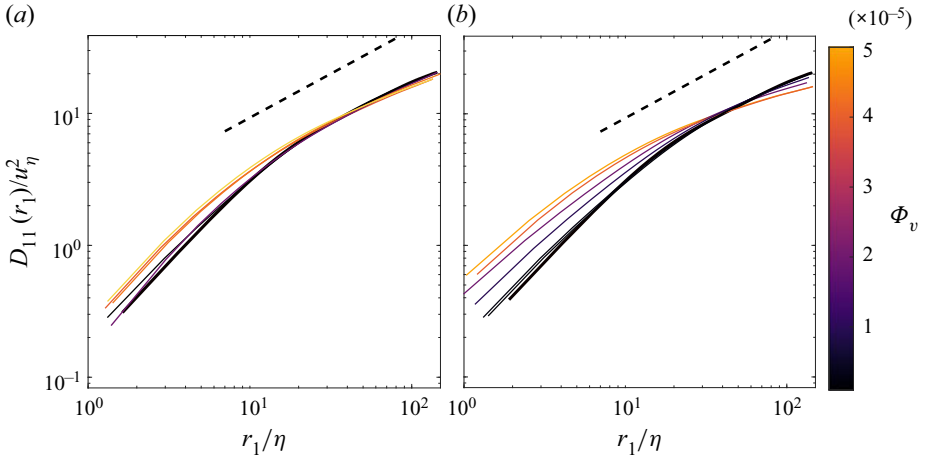

Figure 8. Longitudinal second-order structure functions of the u_1 component for the different volume fractions for (*a*) $St_\eta = 0.3$ and (*b*) $St_\eta = 2.6$. The dashed line indicates the $r^{2/3}$ scaling predicted by Kolmogorov (1941) in the inertial range. The data are from the small FOV.

this picture profoundly. In keeping with the pivoting effect, the energy becomes more evenly distributed across the scales as the particle loading increases: the dispersed phase intercepts part of the fluid momentum at the large scales, and injects it back into the fluid at small scales. The effect is already visible for $St_\eta = 0.3$ and is apparent for $St_\eta = 2.6$.

The cross-over separation r_c, i.e. the separation corresponding to the pivoting point, does not vary significantly with Φ_v, and lies in the ranges 30η–40η and 40η–50η for the lower and higher St_η, respectively. This difference could be a St_η effect or a Re_λ effect. The latter would be consistent with the proposal of Sundaram & Collins (1999) that r_c scales with λ, while the former is at odds with the notion that r_c decreases with St_η (Poelma & Ooms 2006). This conclusion, however, was based on simulations neglecting gravity, which here is crucial to the two-way coupling. Determining a specific trend for r_c would require further measurements with different Sv_η and a broader range of St_η. We do note that the range of scales where the fluctuating fluid energy is increased roughly corresponds to the size of the particle clusters in this regime (Petersen *et al.* 2019).

Finally, the redistribution of the turbulent energy with increasing particle loading can be appreciated by considering the nonlinear inter-scale energy transfer rate, Π. Starting from the Kármán–Howarth–Monin equation (Monin, Yaglom & Lumley 1975), we recently performed such an analysis for the single-phase turbulence in this same facility (Carter & Coletti 2018; see also Lamriben, Cortet & Moisy 2011; Gomes-Fernandes, Ganapathisubramani & Vassilicos 2015; Portela, Papadakis & Vassilicos 2017; among others). Briefly, given two points $\mathbf{x}$ and $\mathbf{x}''$ associated with velocity fluctuations u_i and u_i'' and separated by $\mathbf{r}$, one considers the difference $\delta u_i = u_i - u_i''$ and the associated energy $\delta q_i = \delta u_i \delta u_i$. (Assuming small-scale axisymmetry, as in Carter & Coletti (2018), or isotropy leads to similar values and analogous conclusions.) The radial component of the nonlinear inter-scale energy transfer rate, $\Pi_r = \frac{1}{4}[(\partial/\partial r)(\langle \delta u_i\, \delta q_i^2 \rangle r_i/r) + 1/r^2 \langle \delta u_i\, \delta q_i^2 \rangle r_i]$, is the only one making a net contribution in spherical coordinates. Thus, over the inertial range in single-phase turbulence, the average of Π_r across all orientations in scale space is expected to balance the two-point kinetic energy dissipation ϵ_r (which in the present homogeneous flow

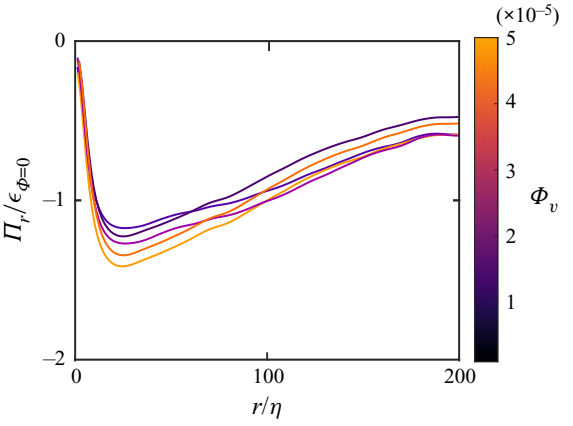

Figure 9. Nonlinear inter-scale energy transfer rate, normalized by the turbulent dissipation and plotted as a function of the scale separation r, at the different particle volume fractions and for the $St_\eta = 2.6$ case. The dissipation from the unladen case is used to normalize all line plots; using ϵ from the individual particle-laden cases corroborates the observed trend of inter-scale transfer increasing with volume fraction. The data are from the small FOV.

coincides with the standard dissipation ϵ). This is confirmed in figure 9, where the ratio $\Pi_r/\epsilon_{\Phi=0}$ is plotted as a function of r for $St_\eta = 2.6$. The negative sign of Π_r indicates the expected direction of the energy cascade from larger to smaller scales, and the values of the ratio close to -1 for $r/\eta \approx 20$–100 reflect the Π–ϵ equilibrium in the inertial range of the unladen turbulence. With increasing particle loading, the magnitude of Π_r in the same range grows significantly. This indicates that with increasing loading, the energy injected at the large scales is being transferred more effectively down the spectral pipeline towards the smaller scales. On the one hand, this is consistent with the observation that particles cause the energy to pivot towards a more even distribution across all scales, as illustrated in figure 8. On the other hand, it points to a specific mechanism by which such redistribution is realized, i.e. the enhancement of the energy cascade. The precise dynamics by which this is realized (e.g. by clusters accelerating the breakdown of large eddies, rather than high-concentration sheets causing instabilities; Kasbaoui, Koch & Desjardins 2019) remains to be clarified, but it is likely specific to the present regime. In fact, particle-resolved DNS (PR-DNS) from Schneiders *et al.* (2017) found that Kolmogorov-scale particles dampened the inter-scale energy flux in the absence of gravity.

In this multi-scale and two-way coupled system, the question of the inter-scale energy transfer is complex, and other interpretations of the results are possible. For example, the enhancement of Π_r might be seen as a mere consequence of the energy added to the fluid by the falling particles, rather than by an intensification of the cascade. In such a scenario, however, one would expect a scale-independent shift of the energy spectrum, as opposed to the observed pivoting. Likewise, the increase of fluctuating energy at small scales could be due solely to the local action of the particles. If this were the case, however, such energy augmentation would be limited to scales much smaller than the range that appears affected. In conclusion, the present interpretation appears consistent with the ensemble of the experimental observations, but further data and analysis are required to make it more conclusive.

4. Conclusions

We have performed a systematic experimental study of turbulence modification by sub-Kolmogorov heavy particles. These are in the range $St_\eta = O(1)$, $\rho_p/\rho_f = O(10^3)$ that has attracted attention for decades, due to its relevance to countless applications and the rich interaction with the flow. With $Re_\lambda \approx 150$–300, the scale separation of the turbulence is enough to display the hallmarks of Kolmogorov's phenomenology, also possessing a high degree of homogeneity over scales much larger than the energetic eddies. The settling velocity parameter $Sv_\eta = O(1)$ is the natural consequence of terrestrial gravity, and separates the present regime from the zero-gravity cases that have formed the bulk of the numerical studies in the literature. By varying incrementally the particle volume fraction, $\Phi_v \approx 10^{-6}$–5×10^{-5}, while keeping all other parameters constant, we have isolated the profound flow modifications caused by the two-way coupling between both phases. We considered both cases $St_\eta < 1$ and $St_\eta > 1$, which behave similarly, the latter producing more marked changes in the carrier phase.

We find that the presence of settling inertial particles leads to the horizontal contraction and vertical elongation of the correlation length of the turbulent fluctuations, in agreement with the observation of Ferrante & Elghobashi (2003) that falling particles stretch vortical structures. The r.m.s. velocity fluctuations, however, are more strongly excited in the horizontal than in the vertical direction. Both components are significantly augmented, and overall the TKE is dramatically increased (roughly doubled) at the higher loadings. This is attributed to the role of gravity: falling particles release their potential energy to the fluid, proportionally to their mass fraction and settling velocity. At the largest volume fractions considered, such energy input rate is comparable to the hydrodynamic forcing of the turbulence (in the present case, from actuated jets).

The velocity structure functions confirm that the presence of particles leads to a redistribution of energy across the spectrum: the turbulence activity is intensified at the small scales and dampened at the large scales, with a cross-over scale around 40η. The two-point analysis shows further that the inter-scale energy flux is enhanced with increasing particle loading. Thus the pivoting of the energy spectrum is rooted in an intensification of the direct energy cascade. The identification and quantification of this process will be important to devise successful (subgrid-scale and/or point-particle) models able to capture the turbulence modification.

In most previous experimental studies, which focused on massively inertial particles ($St_\eta = O(10^2)$), turbulence was found to attenuate TKE. Unlike those cases, the present class of particles exhibits distinct phenomena such as clustering and enhanced settling (as measured in the present facility by Petersen *et al.* (2019) and Berk & Coletti (2021)). The difference in the net variation of TKE depending on the particle inertia may then be due to the time scale associated to the energy input, which in turn is related to the particle dynamics.

While we mainly attribute to St_η the different TKE modification with respect to previous studies, the particle size may also play a role: in most past experiments that found a reduction of TKE, $dp/\eta \approx 1$ or larger (Hwang & Eaton 2006*a*; Tanaka & Eaton 2008; Bellani *et al.* 2012), while here $dp/\eta = O(10^{-1})$. To discern and quantify geometric effects on the flow, particle-resolving simulations are needed, although the present regime is especially challenging to PR-DNS.

It is important to point out that the present findings are applicable to the considered type of particles, i.e. sub-Kolmogorov spheres much denser than the carrier fluid. While this class has been the centre of attention in early particle-laden turbulence studies, more recently numerical and experimental works have often considered much larger and less

dense particles (Qureshi *et al.* 2007; Bellani *et al.* 2012; Uhlmann & Doychev 2014; Fornari *et al.* 2016; Baker & Coletti 2019). Bridging the gap between the two extrema of the parameter space will be important to reach a comprehensive view of the two-way coupling problem (Brandt & Coletti 2022). Experimentally, an obvious obstacle on such a path will be the difficult optical access in highly concentrated particle suspensions, especially at density ratios for which refractive index matching is not an option. Recently, Fong & Coletti (2022) demonstrated that back-lighting can provide quantitative insight in cluster-induced turbulence at Φ_v approaching 10^{-2}, but did so in a relatively confined configuration and could not access the local fluid velocity. Depending on the media, non-optical techniques such as ultrasound imaging velocimetry (Poelma 2017) and X-ray (Aliseda & Heindel 2021) may provide attractive alternatives.

Funding. This work was funded by the US Department of Defense through the Office of Naval Research and the Army Research Office.

Declaration of interests. The authors report no conflict of interest.

Author ORCIDs.
Roumaissa Hassaini https://orcid.org/0000-0003-4501-5305;
Filippo Coletti https://orcid.org/0000-0001-5344-2476.

References

Adrian, R.J. & Westerweel, J. 2011 *Particle Image Velocimetry*. Cambridge University Press.

Aliseda, A. & Heindel, T.J. 2021 X-ray flow visualization in multiphase flows. *Annu. Rev. Fluid Mech.* **53**, 543–567.

Andersson, H.I., Zhao, L. & Variano, E.A. 2015 On the anisotropic vorticity in turbulent channel flows. *J. Fluids Engng* **137** (8), 084503.

Baker, L.J. & Coletti, F. 2019 Experimental study of negatively buoyant finite-size particles in a turbulent boundary layer up to dense regimes. *J. Fluid Mech.* **866**, 598–629.

Baker, L.J. & Coletti, F. 2021 Particle–fluid–wall interaction of inertial spherical particles in a turbulent boundary layer. *J. Fluid Mech.* **908**, A39.

Baker, L.J., Frankel, A., Mani, A. & Coletti, F. 2017 Coherent clusters of inertial particles in homogeneous turbulence. *J. Fluid Mech.* **833**, 364–398.

Balachandar, S. & Eaton, J.K. 2010 Turbulent dispersed multiphase flow. *Annu. Rev. Fluid Mech.* **42**, 111–133.

Balachandar, S., Liu, K. & Lakhote, M. 2019 Self-induced velocity correction for improved drag estimation in Euler–Lagrange point-particle simulations. *J. Comput. Phys.* **376**, 160–185.

Bellani, G., Byron, M.L., Collignon, A.G., Meyer, C.R. & Variano, E.A. 2012 Shape effects on turbulent modulation by large nearly neutrally buoyant particles. *J. Fluid Mech.* **712**, 41–60.

Bellani, G. & Variano, E.A. 2014 Homogeneity and isotropy in a laboratory turbulent flow. *Exp. Fluids* **55** (1), 1646.

Berk, T. & Coletti, F. 2020 Transport of inertial particles in high-Reynolds-number turbulent boundary layers. *J. Fluid Mech.* **903**, A18.

Berk, T. & Coletti, F. 2021 Dynamics of small heavy particles in homogeneous turbulence: a Lagrangian experimental study. *J. Fluid Mech.* **917**, A47.

Boivin, M., Simonin, O. & Squires, K.D. 1998 Direct numerical simulation of turbulence modulation by particles in isotropic turbulence. *J. Fluid Mech.* **375**, 235–263.

Bosse, T., Kleiser, L. & Meiburg, E. 2006 Small particles in homogeneous turbulence: settling velocity enhancement by two-way coupling. *Phys. Fluids* **18** (2), 027102.

Brandt, L. & Coletti, F. 2022 Particle-laden turbulence: progress and perspectives. *Annu. Rev. Fluid Mech.* **54**, 159–189.

Burton, T.M. & Eaton, J.K. 2005 Fully resolved simulations of particle–turbulence interaction. *J. Fluid Mech.* **545**, 67–111.

Capecelatro, J. & Desjardins, O. 2013 An Euler–Lagrange strategy for simulating particle-laden flows. *J. Comput. Phys.* **238**, 1–31.

CARTER, D., PETERSEN, A., AMILI, O. & COLETTI, F. 2016 Generating and controlling homogeneous air turbulence using random jet arrays. *Exp. Fluids* **57** (12), 189.
CARTER, D.W & COLETTI, F. 2017 Scale-to-scale anisotropy in homogeneous turbulence. *J. Fluid Mech.* **827**, 250–284.
CARTER, D.W. & COLETTI, F. 2018 Small-scale structure and energy transfer in homogeneous turbulence. *J. Fluid Mech.* **854**, 505–543.
CISSE, M., HOMANN, H. & BEC, J. 2013 Slipping motion of large neutrally buoyant particles in turbulence. *J. Fluid Mech.* **735**, R1.
CLIFT, R., GRACE, J.R. & WEBER, M.E. 2005 *Bubbles, Drops, and Particles*. Dover Publications.
CROWE, C.T., TROUTT, T.R. & CHUNG, J.N. 1996 Numerical models for two-phase turbulent flows. *Annu. Rev. Fluid Mech.* **28** (1), 11–43.
DE JONG, J., CAO, L., WOODWARD, S.H., SALAZAR, J.P.L.C., COLLINS, L.R. & MENG, H. 2009 Dissipation rate estimation from PIV in zero-mean isotropic turbulence. *Exp. Fluids* **46** (3), 499–515.
EATON, J.K. 2009 Two-way coupled turbulence simulations of gas–particle flows using point-particle tracking. *Intl J. Multiphase Flow* **35** (9), 792–800.
ELGHOBASHI, S. 1994 On predicting particle-laden turbulent flows. *Appl. Sci. Res.* **52** (4), 309–329.
ELGHOBASHI, S. & TRUESDELL, G.C. 1993 On the two-way interaction between homogeneous turbulence and dispersed solid particles. I. Turbulence modification. *Phys. Fluids* A **5** (7), 1790–1801.
ELGHOBASHI, S.E. & ABOU-ARAB, T.W. 1983 A two-equation turbulence model for two-phase flows. *Phys. Fluids* **26** (4), 931–938.
FERRANTE, A. & ELGHOBASHI, S. 2003 On the physical mechanisms of two-way coupling in particle-laden isotropic turbulence. *Phys. Fluids* **15** (2), 315–329.
FONG, K.O., AMILI, O. & COLETTI, F. 2019 Velocity and spatial distribution of inertial particles in a turbulent channel flow. *J. Fluid Mech.* **872**, 367–406.
FONG, K.O. & COLETTI, F. 2022 Experimental analysis of particle clustering in moderately dense gas–solid flow. *J. Fluid Mech.* **933**, A6.
FORNARI, W., PICANO, F. & BRANDT, L. 2016 Sedimentation of finite-size spheres in quiescent and turbulent environments. *J. Fluid Mech.* **788**, 640–669.
FRANKEL, A., POURANSARI, H., COLETTI, F. & MANI, A. 2016 Settling of heated particles in homogeneous turbulence. *J. Fluid Mech.* **792**, 869–893.
GEISS, S., DREIZLER, A., STOJANOVIC, Z., CHRIGUI, M., SADIKI, A. & JANICKA, J. 2004 Investigation of turbulence modification in a non-reactive two-phase flow. *Exp. Fluids* **36** (2), 344–354.
GOMES-FERNANDES, R., GANAPATHISUBRAMANI, B. & VASSILICOS, J.C. 2015 The energy cascade in near-field non-homogeneous non-isotropic turbulence. *J. Fluid Mech.* **771**, 676–705.
GOOD, G.H., IRELAND, P.J., BEWLEY, G.P., BODENSCHATZ, E., COLLINS, L.R. & WARHAFT, Z. 2014 Settling regimes of inertial particles in isotropic turbulence. *J. Fluid Mech.* **759**, R3.
GORE, R.A. & CROWE, C.T. 1991 Modulation of turbulence by a dispersed phase. *J. Fluids Engng* **113**, 304–307.
GUALA, M., LIBERZON, A., HOYER, K., TSINOBER, A. & KINZELBACH, W. 2008 Experimental study on clustering of large particles in homogeneous turbulent flow. *J. Turbul.* **9** (34), 1–20.
GUALTIERI, P., PICANO, F., SARDINA, G. & CASCIOLA, C.M. 2015 Exact regularized point particle method for multiphase flows in the two-way coupling regime. *J. Fluid Mech.* **773**, 520–561.
GUSTAVSSON, K. & MEHLIG, B. 2016 Statistical models for spatial patterns of heavy particles in turbulence. *Adv. Phys.* **65** (1), 1–57.
HORWITZ, J. & MANI, A. 2016 Accurate calculation of Stokes drag for point-particle tracking in two-way coupled flows. *J. Comput. Phys.* **318**, 85–109.
HORWITZ, J. & MANI, A. 2018 Correction scheme for point-particle models applied to a nonlinear drag law in simulations of particle–fluid interaction. *Intl J. Multiphase Flow* **101**, 74–84.
HWANG, W. & EATON, J.K. 2006*a* Homogeneous and isotropic turbulence modulation by small heavy ($St \sim 50$) particles. *J. Fluid Mech.* **564**, 361–393.
HWANG, W. & EATON, J.K. 2006*b* Turbulence attenuation by small particles in the absence of gravity. *Intl J. Multiphase Flow* **32** (12), 1386–1396.
IRELAND, P.J. & DESJARDINS, O. 2017 Improving particle drag predictions in Euler–Lagrange simulations with two-way coupling. *J. Comput. Phys.* **338**, 405–430.
KASBAOUI, M.H., KOCH, D.L. & DESJARDINS, O. 2019 The rapid distortion of two-way coupled particle-laden turbulence. *J. Fluid Mech.* **877**, 82–104.
KHALITOV, D.A. & LONGMIRE, E.K. 2002 Simultaneous two-phase PIV by two-parameter phase discrimination. *Exp. Fluids* **32** (2), 252–268.

KIGER, K.T. & PAN, C. 2000 PIV technique for the simultaneous measurement of dilute two-phase flows. *J. Fluids Engng* **122** (4), 811–818.

KIGER, K.T. & PAN, C. 2002 Suspension and turbulence modification effects of solid particulates on a horizontal turbulent channel flow. *J. Turbul.* **3** (1), 019.

KOLMOGOROV, A.N. 1941 The local structure of turbulence in incompressible viscous fluid for very large Reynolds numbers. *C. R. Acad. Sci. URSS* **30**, 301–305.

KULICK, J.D., FESSLER, J.R. & EATON, J.K. 1994 Particle response and turbulence modification in fully developed channel flow. *J. Fluid Mech.* **277**, 109–134.

LAMRIBEN, C., CORTET, P.P. & MOISY, F. 2011 Direct measurements of anisotropic energy transfers in a rotating turbulence experiment. *Phys. Rev. Lett.* **107** (2), 024503.

LUCCI, F., FERRANTE, A. & ELGHOBASHI, S. 2010 Modulation of isotropic turbulence by particles of Taylor length-scale size. *J. Fluid Mech.* **650**, 5–55.

MATHAI, V., LOHSE, D. & SUN, C. 2020 Bubbly and buoyant particle-laden turbulent flows. *Annu. Rev. Condens. Matter Phys.* **11**, 529–559.

MATSUDA, K., ONISHI, R. & TAKAHASHI, K. 2017 Influence of gravitational settling on turbulent droplet clustering and radar reflectivity factor. *Flow Turbul. Combust.* **98** (1), 327–340.

MAXEY, M. 2017 Simulation methods for particulate flows and concentrated suspensions. *Annu. Rev. Fluid Mech.* **49**, 171–193.

MAXEY, M.R. 1987 The motion of small spherical particles in a cellular flow field. *Phys. Fluids* **30** (7), 1915–1928.

MAXEY, M.R. & RILEY, J.J. 1983 Equation of motion for a small rigid sphere in a nonuniform flow. *Phys. Fluids* **26** (4), 883–889.

MAZZITELLI, I.M., LOHSE, D. & TOSCHI, F. 2003*a* The effect of microbubbles on developed turbulence. *Phys. Fluids* **15** (1), L5–L8.

MAZZITELLI, I.M, LOHSE, D. & TOSCHI, F. 2003*b* On the relevance of the lift force in bubbly turbulence. *J. Fluid Mech.* **488**, 283–313.

MEHRABADI, M., HORWITZ, J., SUBRAMANIAM, S. & MANI, A. 2018 A direct comparison of particle-resolved and point-particle methods in decaying turbulence. *J. Fluid Mech.* **850**, 336–369.

MONCHAUX, R., BOURGOIN, M. & CARTELLIER, A. 2010 Preferential concentration of heavy particles: a Voronoïanalysis. *Phys. Fluids* **22** (10), 103304.

MONCHAUX, R., BOURGOIN, M. & CARTELLIER, A. 2012 Analyzing preferential concentration and clustering of inertial particles in turbulence. *Intl J. Multiphase Flow* **40**, 1–18.

MONCHAUX, R. & DEJOAN, A. 2017 Settling velocity and preferential concentration of heavy particles under two-way coupling effects in homogeneous turbulence. *Phys. Rev. Fluids* **2** (10), 104302.

MONIN, A.S., YAGLOM, A.M. & LUMLEY, J.L. 1975 *Mechanics of Turbulence: Statistical Fluid Mechanics*. The MIT Press.

MYDLARSKI, L. 2017 A turbulent quarter century of active grids: from Makita (1991) to the present. *Fluid Dyn. Res.* **49** (6), 061401.

NASO, A. & PROSPERETTI, A. 2010 The interaction between a solid particle and a turbulent flow. *New J. Phys.* **12** (3), 033040.

NI, R., KRAMEL, S., OUELLETTE, N.T. & VOTH, G.A. 2015 Measurements of the coupling between the tumbling of rods and the velocity gradient tensor in turbulence. *J. Fluid Mech.* **766**, 202–225.

PARIS, A.D. 2001 *Turbulence Attenuation in a Particle-Laden Channel Flow*. Stanford University.

PETERSEN, A.J., BAKER, L.J. & COLETTI, F. 2019 Experimental study of inertial particles clustering and settling in homogeneous turbulence. *J. Fluid Mech.* **864**, 925–970.

POELMA, C. 2017 Ultrasound imaging velocimetry: a review. *Exp. Fluids* **58** (1), 3.

POELMA, C. & OOMS, G. 2006 Particle–turbulence interaction in a homogeneous, isotropic turbulent suspension. *Appl. Mech. Rev.* **59**, 78–90.

POELMA, C., WESTERWEEL, J. & OOMS, G. 2006 Turbulence statistics from optical whole-field measurements in particle-laden turbulence. *Exp. Fluids* **40** (3), 347–363.

POELMA, C., WESTERWEEL, J. & OOMS, G. 2007 Particle–fluid interactions in grid-generated turbulence. *J. Fluid Mech.* **589**, 315–351.

PORTELA, F.A., PAPADAKIS, G. & VASSILICOS, J.C. 2017 The turbulence cascade in the near wake of a square prism. *J. Fluid Mech.* **825**, 315–352.

QURESHI, N.M., BOURGOIN, M., BAUDET, C., CARTELLIER, A. & GAGNE, Y. 2007 Turbulent transport of material particles: an experimental study of finite size effects. *Phys. Rev. Lett.* **99** (18), 184502.

RENSEN, J., LUTHER, S. & LOHSE, D. 2005 The effect of bubbles on developed turbulence. *J. Fluid Mech.* **538**, 153–187.

RIBOUX, G., RISSO, F. & LEGENDRE, D. 2010 Experimental characterization of the agitation generated by bubbles rising at high Reynolds number. *J. Fluid Mech.* **643**, 509–539.

RIGHETTI, M. & ROMANO, G.P. 2004 Particle–fluid interactions in a plane near-wall turbulent flow. *J. Fluid Mech.* **505**, 93–121.

RISSO, F. 2018 Agitation, mixing, and transfers induced by bubbles. *Annu. Rev. Fluid Mech.* **50**, 25–48.

ROGERS, C.B. & EATON, J.K. 1991 The effect of small particles on fluid turbulence in a flat-plate, turbulent boundary layer in air. *Phys. Fluids* A **3** (5), 928–937.

ROSA, B., POZORSKI, J. & WANG, L.P. 2020 Effects of turbulence modulation and gravity on particle collision statistics. *Intl J. Multiphase Flow* **129**, 103334.

SAHU, S., HARDALUPAS, Y. & TAYLOR, A.M.K.P. 2016 Droplet–turbulence interaction in a confined polydispersed spray: effect of turbulence on droplet dispersion. *J. Fluid Mech.* **794**, 267–309.

SAITO, I., WATANABE, T. & GOTOH, T. 2019 A new time scale for turbulence modulation by particles. *J. Fluid Mech.* **880**, R6.

SALIBINDLA, A.K.R., MASUK, A.U.M., TAN, S. & NI, R. 2020 Lift and drag coefficients of deformable bubbles in intense turbulence determined from bubble rise velocity. *J. Fluid Mech.* **894**, A20.

SATO, Y. & HISHIDA, K. 1996 Transport process of turbulence energy in particle-laden turbulent flow. *Intl J. Heat Fluid Flow* **17** (3), 202–210.

SCHNEIDERS, L., MEINKE, M. & SCHRÖDER, W. 2017 Direct particle–fluid simulation of Kolmogorov-length-scale size particles in decaying isotropic turbulence. *J. Fluid Mech.* **819**, 188–227.

SCHRECK, S. & KLEIS, S.J. 1993 Modification of grid-generated turbulence by solid particles. *J. Fluid Mech.* **249**, 665–688.

SQUIRES, K.D. & EATON, J.K. 1990 Particle response and turbulence modification in isotropic turbulence. *Phys. Fluids* A **2** (7), 1191–1203.

SQUIRES, K.D. & EATON, J.K. 1991 Preferential concentration of particles by turbulence. *Phys. Fluids* A **3** (5), 1169–1178.

SUBRAMANIAM, S., MEHRABADI, M., HORWITZ, J. & MANI, A. 2014 Developing improved Lagrangian point particle models of gas–solid flow from particle-resolved direct numerical simulation. In *Studying Turbulence using Numerical Simulation Databases-XV, Proceedings of the CTR*, pp. 5–14.

SUNDARAM, S. & COLLINS, L.R. 1999 A numerical study of the modulation of isotropic turbulence by suspended particles. *J. Fluid Mech.* **379**, 105–143.

TANAKA, T. & EATON, J.K. 2008 Classification of turbulence modification by dispersed spheres using a novel dimensionless number. *Phys. Rev. Lett.* **101** (11), 114502.

TANAKA, T. & EATON, J.K. 2010 Sub-Kolmogorov resolution particle image velocimetry measurements of particle-laden forced turbulence. *J. Fluid Mech.* **643**, 177–206.

TENNETI, S. & SUBRAMANIAM, S. 2014 Particle-resolved direct numerical simulation for gas–solid flow model development. *Annu. Rev. Fluid Mech.* **46**, 199–230.

TOM, J. & BRAGG, A.D. 2019 Multiscale preferential sweeping of particles settling in turbulence. *J. Fluid Mech.* **871**, 244–270.

TOM, J., CARBONE, M. & BRAGG, A.D. 2022 How two-way coupling modifies the multiscale preferential sweeping mechanism. *J. Fluid Mech.* **947**, A7.

UHLMANN, M. & DOYCHEV, T. 2014 Sedimentation of a dilute suspension of rigid spheres at intermediate Galileo numbers: the effect of clustering upon the particle motion. *J. Fluid Mech.* **752**, 310–348.

VARIANO, E.A., BODENSCHATZ, E. & COWEN, E.A. 2004 A random synthetic jet array driven turbulence tank. *Exp. Fluids* **37** (4), 613–615.

VARIANO, E.A. & COWEN, E.A. 2008 A random-jet-stirred turbulence tank. *J. Fluid Mech.* **604**, 1–32.

VREMAN, A.W. 2015 Turbulence attenuation in particle-laden flow in smooth and rough channels. *J. Fluid Mech.* **773**, 103–136.

WANG, G., ABBAS, M. & CLIMENT, É. 2017 Modulation of large-scale structures by neutrally buoyant and inertial finite-size particles in turbulent Couette flow. *Phys. Rev. Fluids* **2** (8), 084302.

WANG, G., FONG, K.O., COLETTI, F., CAPECELATRO, J. & RICHTER, D.H. 2019 Inertial particle velocity and distribution in vertical turbulent channel flow: a numerical and experimental comparison. *Intl J. Multiphase Flow* **120**, 103105.

WANG, G. & RICHTER, D.H. 2019 Two mechanisms of modulation of very-large-scale motions by inertial particles in open channel flow. *J. Fluid Mech.* **868**, 538–559.

WANG, L.P. & STOCK, D.E. 1993 Dispersion of heavy particles by turbulent motion. *J. Atmos. Sci.* **50** (13), 1897–1913.

YANG, T.S. & SHY, S.S. 2005 Two-way interaction between solid particles and homogeneous air turbulence: particle settling rate and turbulence modification measurements. *J. Fluid Mech.* **526**, 171–216.